

High-Bandwidth High-Accuracy Rotary Microactuators for Magnetic Hard Disk Drive Tracking Servos

Toshiki Hirano, Long-Sheng Fan, *Member, IEEE*, Wen Y. Lee, John Hong, Wayne Imano, Surya Pattanaik, *Member, IEEE*, Susanna Chan, Patrick Webb, Roberto Horowitz, *Member, IEEE*, Sanjay Aggarwal, and David A. Horsley

Abstract—This paper reports on the design, fabrication, and testing of an electrostatic microactuator for a magnetic hard disk drive (HDD) tracking servo. First, the design requirements for a microactuator in this application were investigated. These include high Z -directional stiffness, low in-plane stiffness, high structural aspect ratio, large output force, high area efficiency, low cost, and mass production by a batch process. A novel area-efficient rotary microactuator design was devised, and microactuators were successfully fabricated using innovative processing technologies, such as high-aspect-ratio polymer etching and thick metal electrodeposition. The fabricated microactuator has a structural thickness of 40 μm with a minimum gap/structure width of approximately 2 μm (aspect ratio of 20:1). The microactuator's frequency response was measured and it was determined that it can be modeled as a second-order linear system, up to the 26-kHz frequency range. Moreover, the microactuator will enable the design of a servo system that exceeds a 5-kHz servo bandwidth, which is adequate to achieve a track density of more than 25 kilotrack per inch (kTPI). The microactuator/slider assembly was also tested on a spinning disk, with its position controlled by a proportional integral derivative controller using the magnetic position error signal written on the disk. A position accuracy of about 0.05 μm was observed when the servo controller was turned on. This result confirms that this microactuator can be used in a servo system which is capable of more than 25 kTPI. Continuous-time dual-stage servos were designed and simulated using the μ -synthesis technique. A sequentially designed single-input/single-output and a multi-input/multi-output control design method have been shown to be capable of meeting prescribed uncertainty and performance specifications.

Index Terms—Hard disk drive, high-bandwidth servo, microactuator.

Manuscript received March 6, 1998; revised June 7, 1998. Recommended by Guest Editor W. C. Messner. This work was supported in part by the Defense Advanced Research Projects Agency under Contract DABT63-95-C-0028.

T. Hirano, L.-S. Fan, W. Y. Lee, J. Hong, W. Imano, S. Chan, and P. Webb are with the Almaden Research Center, IBM Corporation, San Jose, CA 95120-6099 USA.

S. Pattanaik is with the Storage Systems Division, IBM Corporation, San Jose, CA 95193 USA.

R. Horowitz and S. Aggarwal are with the Department of Mechanical Engineering, University of California at Berkeley, Berkeley, CA 94720-1740 USA.

D. A. Horsley was with the Department of Mechanical Engineering, University of California at Berkeley, Berkeley, CA 94720-1740 USA. He is now with DiCon Fiberoptics, Berkeley, CA 94710 USA.

Publisher Item Identifier S 1083-4435(98)07149-X.

I. INTRODUCTION

THE areal recording density of magnetic hard disk drives (HDD's) has doubled every 18 months and, recently, a density of more than 10 Gb/in² was demonstrated. In order to achieve such high densities, very narrow data tracks are required. Thus, it has become increasingly more difficult to position a magnetic head right on top of narrow data tracks with high accuracy, by using a conventional voice-coil motor (VCM). This is partly due to the hysteresis of the actuator's pivot bearing and the actuator's structural resonant modes, which limit the track-following servo's low-frequency error rejection attenuation and bandwidth. One projection shows that a servo bandwidth of 2 kHz is required to achieve 25 kilotrack per inch (kTPI). However, it is almost impossible to achieve such a high bandwidth using conventional VCM's. To overcome this problem, a dual-stage actuation scheme was devised [1]–[4], which uses a conventional VCM as a coarse, low-bandwidth actuator, and a microactuator as a fine and high-bandwidth actuator (Fig. 1). In this scheme, the microactuator is attached directly on a slider, so that it can compensate for the VCM's structural resonant modes. Moreover, this configuration minimizes the mass which the microactuator has to drive, since the microactuator only needs to move the slider, which has a very low mass (less than 2 mg for current picoslider).

In Section II, we describe the performance requirements that must be met by a microactuator in this application. An electrostatic microactuator design that meets these requirements is presented in Section III. Innovative high-aspect-ratio polymer etching and thick metal electrodeposition fabrication processes are described in Section IV. Experimental results, which describe the operating characteristics of the microactuator, are presented in Section V-B. In Section VI, we present dual-stage servo control design techniques. Conclusions are given in Section VII.

II. MICROACTUATOR REQUIREMENTS

As described in the introduction, the electrostatic microactuator described in this paper was designed to be inserted between the suspension and the slider of a magnetic HDD

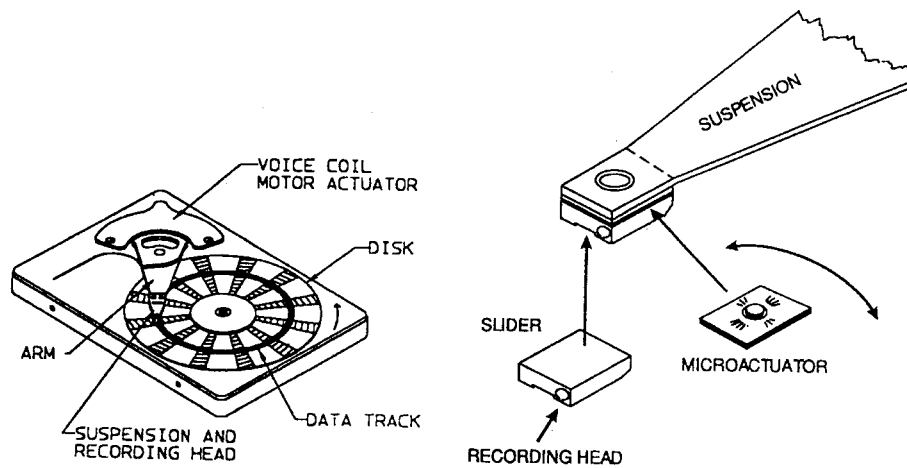


Fig. 1. Piggy-back actuation scheme.

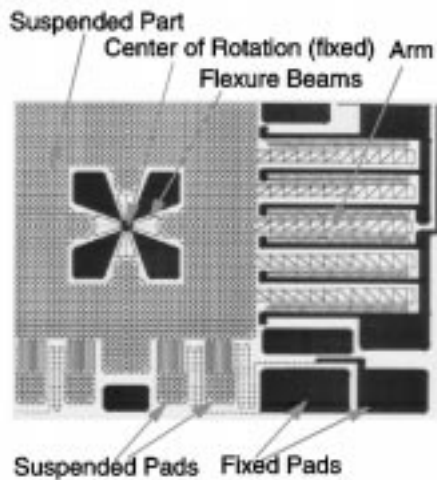


Fig. 2. Rotary actuator design.

unit, in order to move the slider relative to the suspension with a sufficiently high servo bandwidth to attain or exceed a 25-kTPI track density. To achieve this goal, the microactuator must meet several structural and performance requirements. Firstly, it must be flexible in the operational direction of motion (along the data track), but very stiff in vertical and radial directions, to prevent the excitation of resonance modes in these directions. Thus, the structural resonant frequencies in the vertical and radial directions must be much higher than that of the operational direction of motion. In addition, the Z -directional stiffness must be high enough to withstand the loading force that is applied by the suspension beam to the slider. This loading force presses the slider down to the disk surface and is necessary to maintain an adequate air bearing between the slider and the disk surface during operation. Thus, the microactuator must be a high-aspect-ratio structure with a large structural height in order to meet these requirements.

The second requirement is force output. Since the microactuator must drive a slider weighing a few milligrams, and the maximum usable area and driving voltage of the microactuator are limited, an area-efficient design is required.

A high-aspect-ratio structure with a large structural height is also advantageous in this case, since the electrostatic force, which propels the microactuator and slider, is proportional to the structural height of the actuator's stator and rotor electrodes and inversely proportional to the electrodes' gap width. In addition, an area-efficient electrode design is essential to place the maximum number of electrodes in a limited device area.

The third requirement is that the microactuator must be easily assembled with the slider. Since the magnetic head is attached to the slider, which, in turn, is attached to the moving part of the microactuator, and the bonding pads on the slider must be connected to outside electronics, it is necessary to establish electrical connections through the microactuator that are mechanically very flexible.

The last requirement is low manufacturing cost, since these microactuators will be used in HDD's, the market for which is extremely price sensitive. Moreover, microactuator mass production by batch processing is mandatory, since the number of microactuators must be equal to the number of magnetic heads.

III. MICROACTUATOR DESIGN

This section describes a microactuator design that satisfies all of the requirements mentioned above.

A. Rotary Microactuator Design

A rotary microactuator design was employed, because the energy required to rotate the slider is smaller than that which is necessary to translate it. As the magnetic head is attached at the edge of the slider body, a large translational head displacement can be obtained by a relatively small slider angular motion. Another advantage of using a rotary design is that a relatively small dynamic coupling is attained between the VCM input and the microactuator rotational displacement. This is particularly important during the track-seeking motion, when the VCM exerts large accelerations and decelerations on the slider's center of mass.

Fig. 2 shows a typical rotary microactuator design. The center of rotation is fixed to the substrate, which is, in

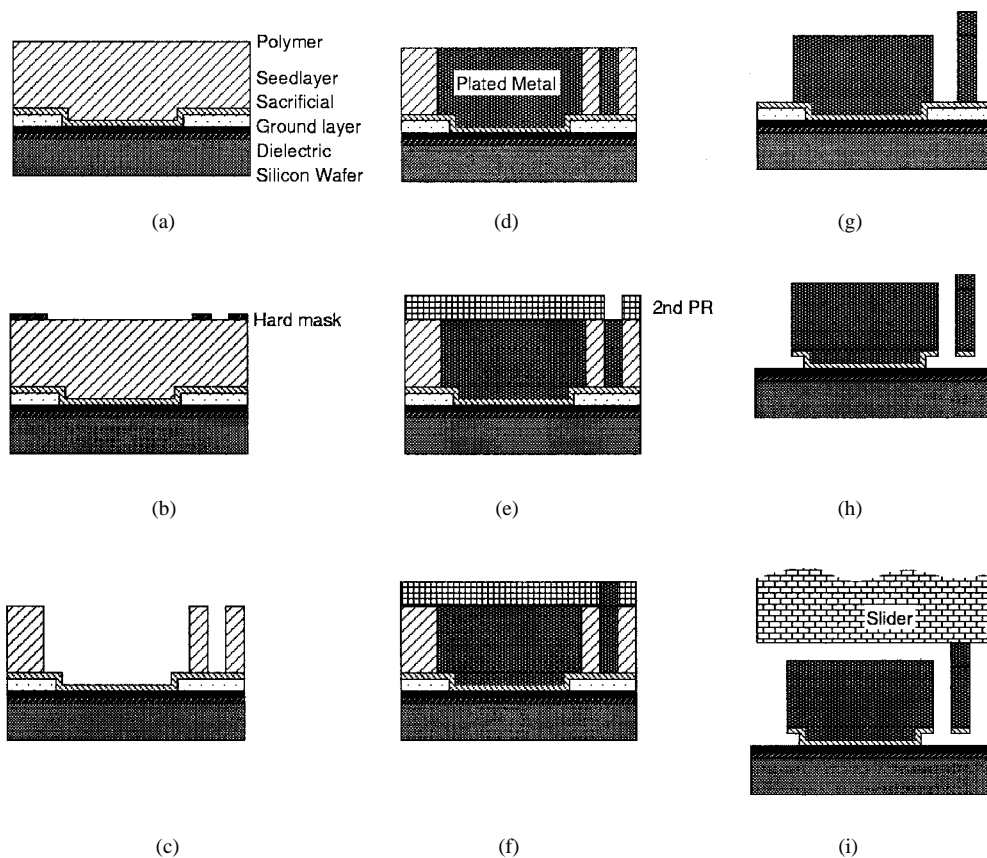


Fig. 3. Fabrication sequence (cross-sectional view).

turn, attached to the suspension's gimbal. The microactuator's moving part, which consists of meshed structures, is suspended by radial flexure beams. The central block, which consists of fine meshes, is where the slider is attached. The radial flexure beams allow only rotational motion to the suspended part. The aspect ratio (the ratio between the width and the height) of these flexure beams must be very high in order to achieve a high Z -directional stiffness and low in-plane (operational direction) rotational stiffness, since the stiffness ratio is proportional to the square of the aspect ratio of the beam. As will be described in Section IV, we have developed a 20:1 aspect ratio process, which theoretically enables a 400:1 flexure stiffness ratio. This enables the microactuator to move over a large range in the operational direction, while, at the same time, minimizing the microactuator's Z displacement due to the Z -directional loading force.

The flexure beams are attached as closely as possible to the center of rotation, since rotational flexibility is maximized in this configuration. Also, temperature effects on the flexure stiffness are minimized, since the whole moving part expands/contracts due to the thermal expansion, at the same rate. Thus, no tension/compression is applied to these beams, even if there is a thermal expansion mismatch between the substrate and the structure.

B. Area-Efficient Electrode Design

We have conceived a novel electrode design, as shown in Fig. 2, to achieve high microactuator areal efficiency. The

interdigitated electrode comb-finger design was employed to obtain a position-independent electrostatic output force. In addition, a differential driving scheme [1] is used to drive the microactuator, which linearizes the voltage/force relationship. These two features are advantageous for high-performance servo control, since they make the microactuator voltage/displacement dynamics linear.

The electrode "fingers" are attached to "arms," which, in turn, are attached to the central body of the moving part (see Fig. 2). The arms are parallel to each other, in order to maintain a constant spacing between them. The conventional radial arm design [1], [5] loses its areal efficiency around the locations that are farther from the center of rotation, since the separation between arms becomes wider there. In the current design, each individual "finger" electrode, which generates an electrostatic force, is attached to the parallel arm with an angle such that the finger is locally orthogonal to the line that connects the finger to the center of rotation. This electrode configuration allows the fingers to generate a pure torque output around the center of the rotation. The same driving voltage is applied to the diagonal electrode set on the other side of the microactuator, which is not shown in the figure. The interelectrode gap width is approximately $3 \mu\text{m}$. This area-efficient electrode design reduces the device area that is necessary to generate the required torque output and, thus, reduces the device cost, which is roughly proportional to device area.

C. Integrated Traces

As indicated in the previous section, the slider is attached to the moving part of the microactuator, and the magnetic read/write heads are riding on the slider. Thus, flexible electrical connections must be established between the slider and the external read/write electronics. Conventional wiring techniques used in the magnetic HDD industry, such as thin-wire ultrasonic attachment, cannot be used to attached wires directly to the slider in this system. These additional wires detrimentally affect the dynamic response of the microactuator/slider assembly and appear as additional resonance modes in the input/output frequency response of the device. To circumvent this problem, we have developed “integrated traces,” which are micromachined flexible electrical connections that are integrated with the microactuator. As shown in Fig. 2, a “suspended” pad is connected to a “fixed” pad, which is rigidly attached onto the substrate, through a meandering structure. This meandering structure establishes the electrical connection between the two pads. The “suspended” pad is eventually connected with a pad on the slider by means of a solder-reflow process. The conventional ultrasonic wire-bonding method can be used on the “fixed” pad to connect a wire to the external electronics, such as the write current driver and read signal amplifier. The meandering structures are designed such that their stiffness is much smaller than that of the central flexure beams.

IV. FABRICATION

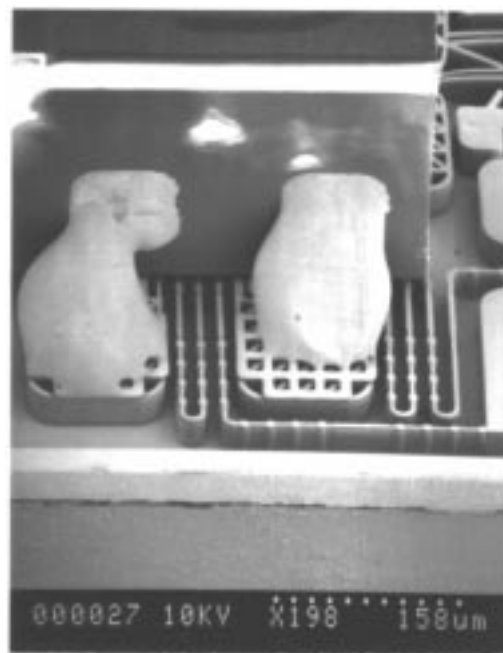
Fig. 3 shows a cross-sectional view of the fabrication sequence. A sacrificial layer (PSG) is deposited on a silicon substrate. This layer is patterned to make an “anchor,” where the structure is fixed to the substrate. The substrate will be eventually attached to a gimbal when the HDD is assembled. After the seed layer is deposited, a thick polymer layer (40 μm) is coated by a single low-revolutions-per-minute spin-coating method [Fig. 3(a)]. A hard mask is patterned on top of the polymer layer [Fig. 3(b)]. Subsequently, the polymer layer is patterned with a high aspect ratio by plasma etching [Fig. 3(c)]. We have developed a process which achieves up to 20:1 aspect ratio, with a fast etch rate of more than 2 $\mu\text{m}/\text{min}$ [6]. After patterning, a thick layer of an iron–nickel alloy is electroplated using the patterned polymer as a mold [Fig. 3(d)] [7]. A photoresist layer is then spun and patterned [Fig. 3(e)], followed by the second metal electroplating [Fig. 3(f)]. This creates the elevated surface that the slider is attached to. Subsequently, the photoresist, the polymer layer, and the seed layer are removed [Fig. 3(g)], and the sacrificial layer is etched with buffered hydrofluoric acid (HF) [Fig. 3(h)]. Finally, the wafer is diced into individual devices, and the slider is attached on top of the moving part of the microactuator [Fig. 3(i)].

A. Fabrication Results

Fig. 4(a) shows an SEM photograph of the fabricated and assembled microactuator. The microactuator’s overall size is 2.7 mm in width and 1.7 mm in length. A picoslider, the size of which is 1 mm in width, 1.25 mm in length, and



(a)



(b)

Fig. 4. SEM photograph of a microactuator assembled with slider and suspension.

0.3 mm in thickness, is attached on top of the microactuator. The microactuator/slider assembly is attached on a “suspension/gimbal” assembly, the other end of which is attached to a VCM. The four wires on the front side of the actuator are for head read/write signals, which are led to the slider via the integrated traces described above. The three wires on the back side of the device are the microactuator drive wires. Fig. 4(b) shows a magnified view of the same assembly. Solder balls are used to connect the microactuator “suspended” pads

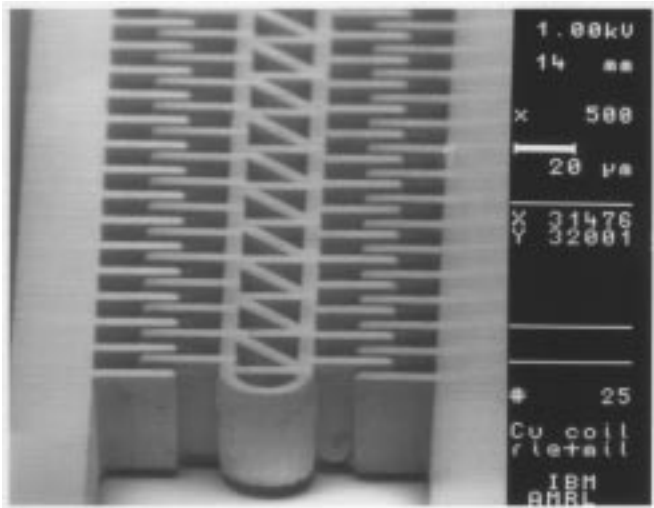


Fig. 5. SEM photograph of electrodes (40-μm thick).

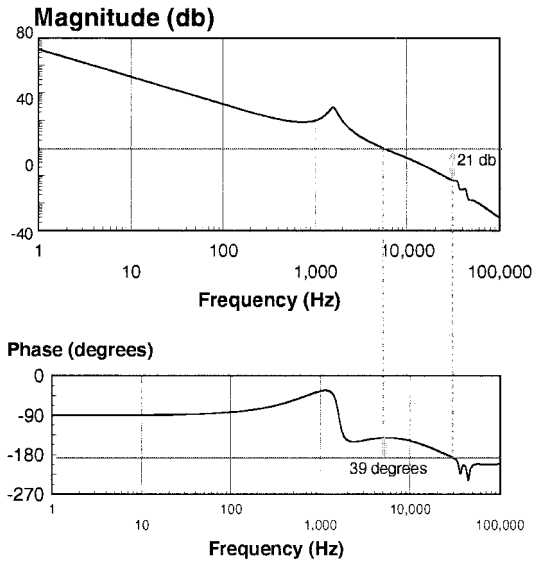


Fig. 7. Calculated open-loop transfer function of the microactuator/PID controller.

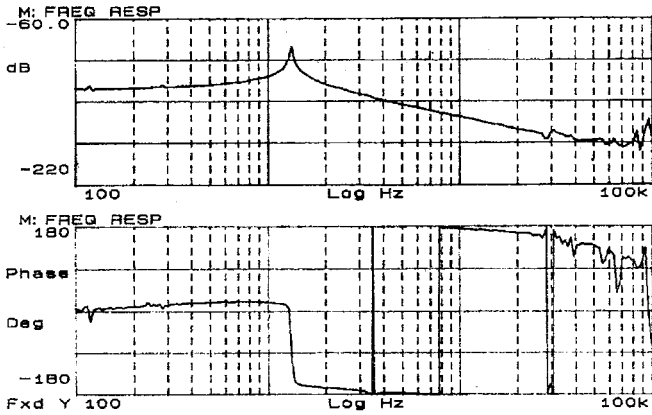


Fig. 6. Frequency response of the microactuator (input: drive voltage; output: displacement measured by LDV).

with the slider pads. Fig. 5 shows a magnified view of the electrode. The microactuator structural height is 40 μm. This particular device has an electrode width of approximately 4 μm and interelectrode gaps of about 3 μm. The high aspect ratio and thick structural height provide both a high Z-directional stiffness and large electrostatic driving force.

V. EXPERIMENTAL RESULTS

A. Microactuator Gain and Stiffness

A microactuator was assembled with a picoslider and tested on a probe station. A driving voltage (large dc bias + small ac) was applied, and its motion was observed under an optical microscope. The resonant frequency was determined by tuning the ac frequency so that the resonant amplitude became maximum. The resonant frequency of this microactuator was 1.37 kHz. Assuming that the rotational inertia of the slider and the microactuator of 0.57×10^{-12} kg·m², the spring constant is calculated to be 42×10^{-6} N·m/rad, which is significantly higher than the designed spring constant (13×10^{-6} N·m/rad).

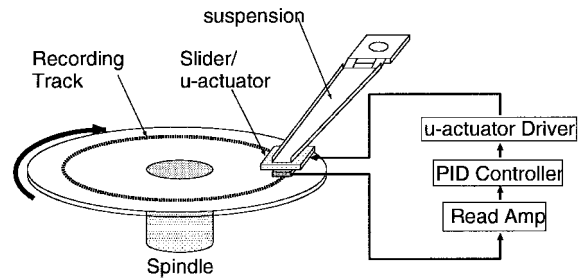


Fig. 8. Experimental setup of servo experiment.

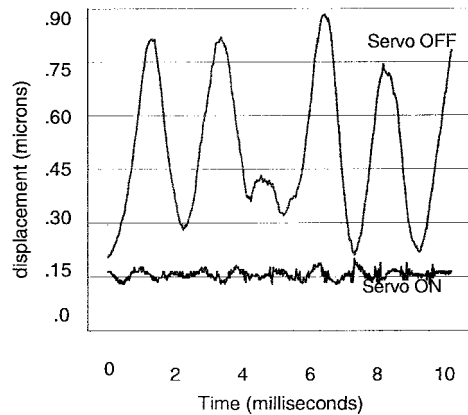


Fig. 9. Position error signal (upper: servo off; lower: servo on).

A part of the difference comes from the “integrated traces” that are attached far from the center of rotation, resulting in a large contribution to the rotational stiffness. The Z-directional stiffness of the suspension can also be calculated to be 4.8×10^5 N/m, which corresponds to the deflection of 0.04 μm at typical 2 gram-force (gf) slider loading force.

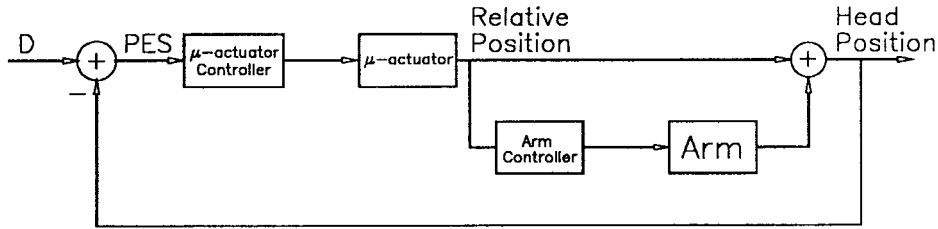


Fig. 10. Sequential SISO controller block diagram.

Electrostatic output torque T can easily be estimated from the electrode geometry, which is expressed by

$$T = \frac{\epsilon h n L V^2}{g} \quad (1)$$

where ϵ is the permittivity of the air, h is the electrode height, n is the number of electrodes, L is the distance between center of the force and the center of rotation, V is the applied voltage, and g is the interelectrode gap. There are 240 electrode fingers with $3\text{-}\mu\text{m}$ gaps. Assuming the maximum voltage of 80 V and L of 1 mm, the maximum torque of this microactuator becomes 1.8×10^{-7} N·m. If we use the spring constant derived above (42×10^{-6} N·m/rad), the maximum displacement at the edge of the slider (the position of magnetic head) is $2.7 \mu\text{m}$, which is adequate to cover two adjacent tracks on both sides at 25 kTPI track pitch.

B. Servo Control Results

The open-loop frequency response of the microactuator/slider assembly was measured using a Laser Doppler Vibrometer (LDV). Fig. 6 shows the resulting Bode plot. The microactuator/slider assembly's first resonance mode is at 1.3 kHz, and it corresponds to the assembly's spring-mass mode. Beyond the 1.3-kHz resonance frequency, the Bode plot gain decreases with a very smooth 40 dB/decade slope, and the phase remains close to -180° (or $+180^\circ$) up to a very high frequency (approximately 80 kHz), without revealing the presence of any major higher order resonant mode. Thus, the microactuator/slider assembly can be accurately modeled by a simple mass-spring-damper second-order system, and is an ideal open-loop dynamics for realizing a very high closed-loop servo bandwidth. Fig. 7 shows the calculated open-loop transfer function's Bode plot when a simple proportional integral derivative (PID) control feedback system is closed around the microactuator/slider assembly's displacement. This calculation shows that the PID servo system's control loop can be closed with a 5-kHz gain crossover frequency and large phase and gain margins of 39° and 21 dB, respectively. This represents almost a factor of ten improvement in terms of bandwidth over existing VCM servo systems, the typical bandwidth of which are around 500 Hz. It has been projected that a 2-kHz servo bandwidth will be necessary to achieve 25 kTPI. Thus, this microactuator should have an adequate performance to meet and exceed this requirement.

A closed-loop servo experiment was conducted using a microactuator/slider/suspension assembly and a spinning disk,

on a spindstand. Fig. 8 shows the experimental setup. The root of the suspension beam was fixed, in order to test the microactuator's performance only. The slider flew on the spinning magnetic disk, which had a prewritten magnetic position signal. The magnetic head on the slider was used to sense the position error signal (PES) between the track on the disk and the position of the sensor. The PES was then fed back to the microactuator. The simple PID controller described above was used to compensate for the position error. Fig. 9 shows time-domain PES data. The upper curve shows the PES signal when the servo is off, and the lower curve shows the corresponding signal under closed-loop control. The large vibrations shown in the top curve, which are due to the first resonance mode of the microactuator flexure, were effectively suppressed by the feedback controller, and the PES was substantially reduced. The closed-loop PES is less than $0.05 \mu\text{m}$, which is adequate to achieve 25 kTPI ($1\text{-}\mu\text{m}$ track pitch).

VI. DUAL-STAGE SERVO DESIGN

A dual-stage track-following servo system requires a more sophisticated controller than that of a conventional single-stage servo system. At low frequencies, where the magnitude of the track runout tends to be large, tracking must be done primarily by the VCM of the HDD and the suspension/gimbal assembly, which will be referred to as the "arm." However, the microactuator is still capable of performing some level of low-frequency fine positioning to compensate for frictional disturbances, the hysteresis of the VCM's pivot bearing, and windage, which limit the low-frequency positioning accuracy of the arm. At higher frequencies, where the magnitude of the track runout is smaller and structural resonances limit the capabilities of the arm, most of the tracking should be performed by the microactuator.

Two continuous-time control synthesis approaches, both based on the μ -synthesis technique [10], were investigated. The first exploits the fact that the dynamics of the microactuator are sufficiently decoupled from that of the VCM and arm, since the microactuator inertia and force output are over 100 times smaller than those of the VCM and arm, and the microactuator suspension is sufficiently stiff. As a consequence, it is assumed that the control input to the VCM has no effect on the relative position between the microactuator and the VCM and arm. In this approach, two single-input/single-output (SISO) compensators are sequentially designed. The first compensator, which has as its input the position of the microactuator relative

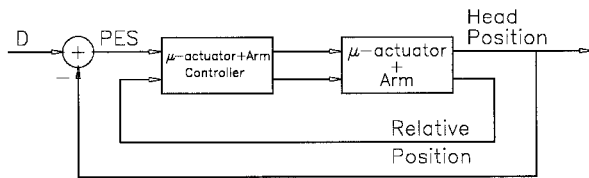


Fig. 11. MIMO controller block diagram.

to the arm and generates a control signal for the VCM, is designed as if it was to be used in a conventional single-stage servo system. The second compensator, which has as its input the PES of the head relative to the track and generates a control signal for the microactuator, is designed accounting for the fact that the first compensator is acting on the VCM and stabilizes the overall closed-loop dynamics. This design approach is also referred to as the *master-slave approach*, since the VCM compensator attempts to make the arm follow the microactuator, while the microactuator compensator attempts to minimize the PES. A block diagram of the control system is shown in Fig. 10.

The second control structure is a multi-input/multi-output (MIMO) design, which takes full account of the coupling between the arm and microactuator. A block diagram of the control system is shown in Fig. 11.

The dual-stage disk drive model used for the controller design and simulation is shown in Fig. 12. Here, a linear displacement model is shown for simplicity. This simple system attempts to model the rigid body mode of the positioning system, the most significant resonance mode of the arm's suspension which is generally the first torsional mode, and dynamics of the microactuator's suspension. The parameters used in the system model were chosen mostly based on data obtained from commercial drives and the microactuator experiments described in the previous section. The torsional resonance of suspension was assumed to be at 2.0 kHz and to have a damping ratio of 0.01. For the microactuator, the resonance due to the combination of the mechanical and electrical spring stiffnesses was placed at 1.0 kHz, and the damping ratio was chosen as 0.5. The damping is due to drag forces which act on the slider as it flies over the disk surface on an air bearing. Unfortunately, at the time when the design was made, no one had studied or measured the rotational or lateral dynamics of the slider relative to the suspension. To roughly model the effect of bearing stiction, the input to the arm was passed through a second-order high-pass filter with a cutoff of 60 Hz. In this way, the control input to the arm is attenuated below 60 Hz, which is the approximate threshold of bearing friction effects on many drives.

MATLAB's μ -synthesis toolbox [10] was used to design the compensators for the dual-stage servo systems. The block diagram used for the design is shown in Fig. 13. The figure shows the weighting blocks that were used to define the performance and robustness specifications. Although only the MIMO model is shown, the same weightings were used for the sequential SISO design. As shown in Fig. 13, a fictitious primed track runout input D' of unity infinity norm is scaled by a frequency-dependent weight W_D to generate the actual

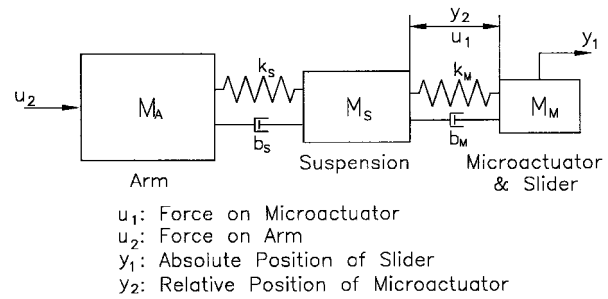


Fig. 12. Control system model.

track runout D . The actual PES signal and the microactuator's relative position are, respectively, weighted by static gains W_{E1} and W_{E2} to generate the test outputs $E1$ and $E2$. The design approach is based on the fact that the μ -synthesis design algorithm of the toolbox attempts to converge, through an iterative process, to a feedback system which has a unity closed-loop infinity norm from D' to the test outputs. To achieve meaningful control systems designs, the weightings W_D , W_{E1} , and W_{E2} must be selected so that the spectrum of the model's runout D approximates that of an actual disk nonrepeatable runout and the infinity norms of both the PES and microactuator's relative position signal are within allowable values when the test outputs $E1$ and $E2$ have unity infinity norms.

In general, to keep the overall system model order and resulting controller order low, weightings of at most second order were used in the design. The second-order disturbance weighting W_D is shown in Fig. 14. This particular weighting was chosen to simulate the spectrum of an actual nonrepetitive track runout in a disk drive, which is expected to have a large low-frequency component, with a steady decrease in magnitude for increasing frequency [11]. The specific low-frequency magnitude and the roll-off frequency were chosen such that, when combined with W_{E1} and W_{E2} , the low-frequency disturbance attenuation is 48 dB for the PES and 32 dB for the microactuator position, and the bandwidth is greater than 800 Hz for the PES and greater than 225 Hz for the microactuator position, as discussed below. For W_{E1} and W_{E2} , constant values were used. To leave some room for error in the disturbance weighting specification, W_{E1} divided the PES by 80 nm, and W_{E2} divided the microactuator position by 0.5 μm .

To achieve robust performance and limit the bandwidth of the control system within realistic bounds, modeling uncertainty weightings were incorporated in the block diagram. As shown in Fig. 13, the uncertainty weights W_{U1} and W_{U2} respectively act on the arm torque (τ_{ARM}) and microactuator torque (τ_{ACT}) to produce a control input uncertainty. These input uncertainties are respectively scaled by the gains d_1 and d_2 . The net effect is to produce a frequency-dependent percentage uncertainty on the control input. The specific first-order weights W_{U1} and W_{U2} used in the control design are shown in Fig. 15. For both the arm and microactuator, the uncertainty starts at 5% at low frequencies, and it increases to 100% at high frequencies. In general, the transition away from

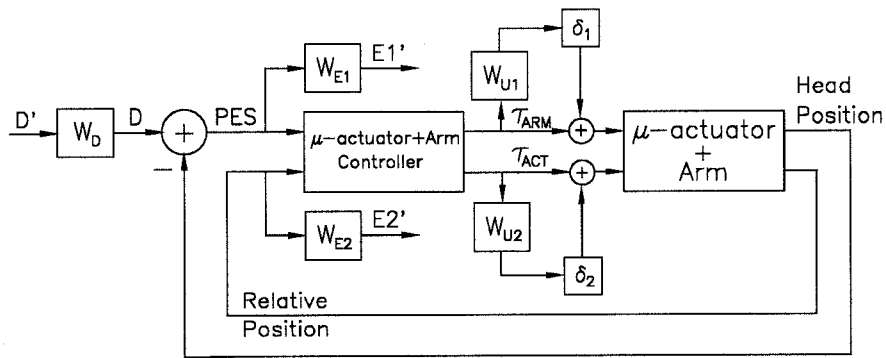
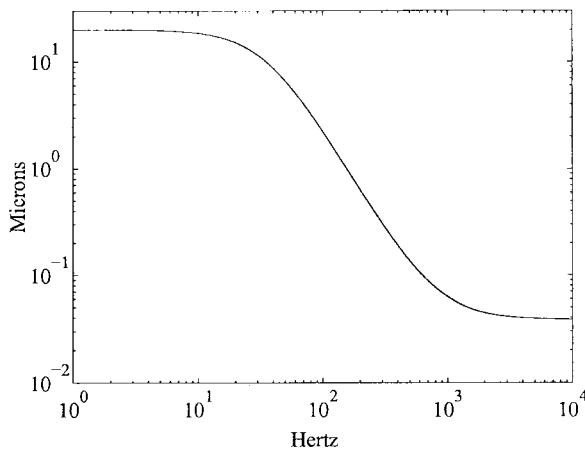


Fig. 13. Structured disturbance and uncertainty models.

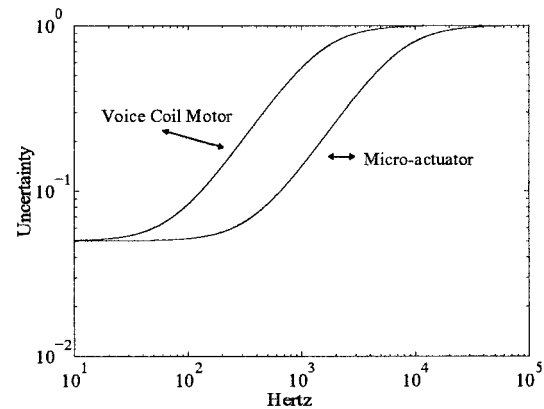
Fig. 14. Runout weight W_D used for μ -tools design.

5% uncertainty was chosen to occur in the neighborhood of the desired bandwidths for the arm and microactuator. Thus, both the arm and the microactuator are assumed to be accurately modeled up to their respective desired closed-loop bandwidths. For the arm, the 20% uncertainty point is at 300 Hz and, at 2 kHz, where its first mechanical resonance is located, the uncertainty is nearly 100%. For the microactuator, there is 20% uncertainty at 1.5 kHz. A general rule of thumb, which was determined from the controller design obtained, is that the closed-loop bandwidth of both the arm and the microactuator roughly corresponds to the 20% uncertainty point.

Readers are referred to [9] and [8] for further details on the design methodology and weightings selection.

A. Control Design Results

The closed-loop PES sensitivity transfer functions for both the sequential SISO and MIMO dual-stage servo designs are shown in Fig. 16. The PES sensitivity transfer function of the single-stage servo, designed for the arm alone in the first stage of the sequential SISO approach, is also shown in Fig. 16. This plot is shown in order to compare the dual-stage results with a single-stage servo system. The closed-loop transfer functions from the track runout to the microactuator relative position for both dual-stage servo designs are shown in the right-hand side of Fig. 17. A key feature of the PES transfer functions is that, while the single-stage design flattens out at 60 Hz due

Fig. 15. Control input uncertainty used for arm (W_{U1}) and microactuator (W_{U2}).

to bearing friction, the microactuator enables the dual-stage designs to continue increasing the attenuation beyond 60 Hz, resulting in an increased low-frequency attenuation of 25 dB relative to the single-stage design. The single-stage controller achieves a low-frequency PES disturbance attenuation of 33 dB with a six-state controller and a bandwidth of 400 Hz. Both the MIMO and SISO controllers have a low-frequency PES disturbance attenuation of 59 dB. The MIMO controller uses only a nine-state controller and achieves a bandwidth of 3.0 kHz. The SISO design, on the other hand, requires a 13-state controller (six for the arm and seven for the microactuator) and achieves a bandwidth of 2.0 kHz. For each of the controllers, order reduction was performed by eliminating some of the states with the smallest Hankel singular values [10]. The control order for both the MIMO and SISO designs was the minimum achievable while still maintaining robust performance. This was tested by checking that the μ value of the closed-loop system was still less than unity for the reduced-order controllers.

As an additional measure of robustness for each of the designs, the phase and gain margins for each controller was determined. The open-loop phase margin for the single-stage design is 52° , with a gain margin of 23 dB. For the MIMO and SISO designs, the margins were determined by breaking the feedback from the head position and then looking at the open-loop transfer function from PES to head position. For the MIMO design, a phase margin of 60° is achieved with a gain margin of 60 dB. The corresponding SISO margins are 65° and

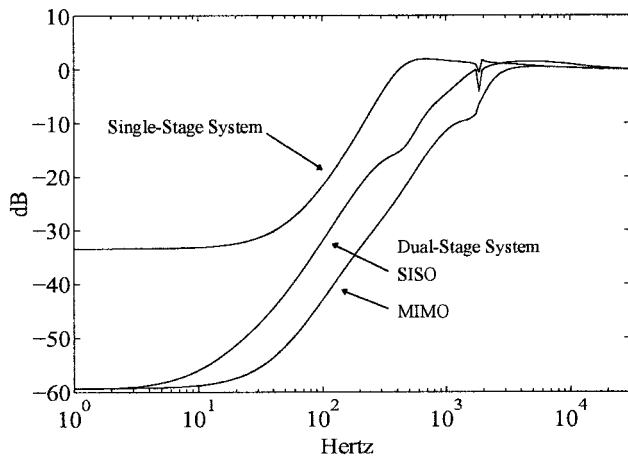


Fig. 16. Closed-loop PES sensitivity transfer functions for SISO and MIMO designs.

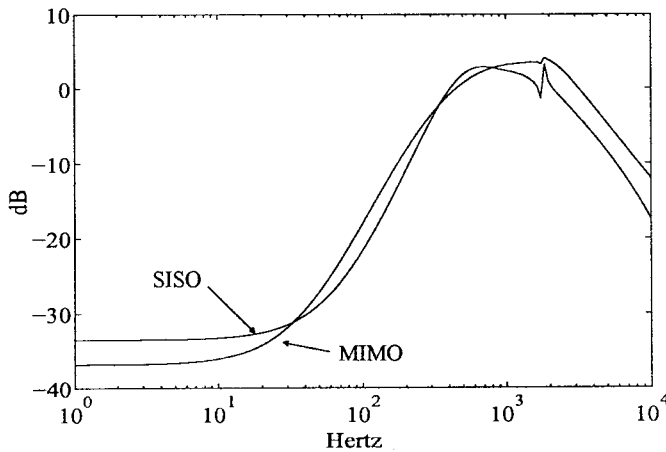


Fig. 17. Runout to microactuator relative position transfer function for SISO and MIMO designs.

24 dB. The microactuator track runout tracking is very similar in both the SISO and MIMO designs. For both the SISO and MIMO designs, the relative position transfer function is near 0 dB from 400 Hz to the system bandwidths of 2.0 and 3.0 kHz, respectively. This region represents the frequencies over which tracking is done primarily by the microactuator, since, in this frequency region, the relative position is approximately equal to the track runout.

For the SISO design, the low-frequency attenuation from track runout to relative position is 33 dB, and for the MIMO design it is 37 dB. In this region, tracking is done primarily by the arm. However, in order for the dual-stage servo to achieve the full runout to PES low-frequency attenuation shown in Fig. 16, some additional tracking is performed by the microactuator in the low-frequency region. For both the SISO and MIMO designs, the relative position transfer function is near 0 dB from 400 Hz to the system bandwidths of 2.0 and 3.0 kHz, respectively. This region represents the frequencies over which tracking is done primarily by the microactuator, since, in this frequency region, the relative position is approximately equal to the track runout. A final feature of both the PES and microactuator position transfer functions is the small notch that occurs at the suspension resonance. Although it is more

significant in the SISO design, it occurs to some extent in both designs. This is due to the fact that the controller attempts to cancel the resonance, but cannot do so perfectly, due to the model uncertainty. As a result, some residual effect is seen in the nominal transfer function. Nevertheless, over the specified range of uncertainty, the μ -tools design guarantees that the system will remain stable and achieve the performance specifications.

VII. CONCLUSION

An electrostatic microactuator, which can be used on a 25-kTPI dual-stage tracking servo system for magnetic HDD's, was studied. First, the requirements that the microactuator must satisfy were investigated, including stiffness, output force, head signal transmission, and cost. A novel microactuator design was presented which satisfies these requirements. The microactuator was successfully fabricated and assembled by using unique microfabrication and assembly techniques, including high-aspect-ratio polymer etching and thick metal electrodeposition. The microactuator was experimentally tested, and its performance was verified. Experimental results confirm that the microactuator under feedback control can achieve a closed-loop bandwidth of approximately 5 kHz, which is adequate to achieve 25 kTPI. A microactuator/slider/suspension assembly was also tested on a spinning disk, and a position error of 0.05 μm was observed when the servo control was turned on. This result also confirms that the microactuator can operate in a 25-kTPI dual-stage tracking servo system.

Continuous-time dual-stage servos have been designed using the μ -synthesis technique. Sequential SISO and MIMO designs have been shown to be capable of meeting the prescribed uncertainty and performance specifications. The MIMO design achieved a simulated low-frequency disturbance rejection of 59 dB and a bandwidth of 3.0 kHz

ACKNOWLEDGMENT

The authors wish to thank S. Arya for supplying parts used in the experiment, D. Tigges for the electrical circuits which are used in the servo experiment, and F. Scott for the assembly of the microactuator. A part of the research presented in this paper was a collaborative work of the authors with Prof. A. Packard and Prof. A. P. Pisano at the University of California at Berkeley.

REFERENCES

- [1] L.-S. Fan, S. J. Woodman, R. C. Moore, L. Crawforth, T. C. Reiley, and M. A. Moser, "Batch-fabricated area-efficient milli-actuator," in *Proc. Solid-State Sensor and Actuator Workshop*, Hilton Head, SC, 1994, pp. 38-42.
- [2] W. Tang, R. Miller, A. Desai, V. Temesvary, S. Wu, W. Hsieh, Y. Tai, and D. Miu, "Silicon micromachined electromagnetic microactuators for rigid disk drives," in *Proc. INTERMAG'97*, 1995, p. ED-08.
- [3] T. Hirano, L.-S. Fan, J. Gao, and W. Lee, "MEMS milli-actuator for hard-disk drive tracking servo," *IEEE J. Microelectromech. Syst.*, vol. 7, no. 2, pp. 149-155, June 1998.
- [4] D. Horsley, A. Singh, A. Pisano, and R. Horowitz, "Angular micropositioner for disk drives," in *Proc. IEEE MEMS'97*, Jan. 1997, pp. 454-459.
- [5] W. C. Tang, T. C. Nguyen, and R. T. Howe, "Laterally driven polysilicon resonant microstructures," in *Proc. IEEE MEMS'89*, 1989, pp. 53-59.

- [6] J. Gao, W. Lee, T. Hirano, and L.-S. Fan, "High aspect ratio etching in polymer for microactuator application," in *Proc. Micromachining and Microfabrication Process Technology'97*, 1997, pp. 110–117.
- [7] T. Hirano and L.-S. Fan, "Invar electrodeposition for MEMS application," in *Proc. SPIE Symp. Micromachining and Microfabrication*, Austin, TX, Oct. 1996, pp. 252–259.
- [8] S. Aggarwal, "Design and control microactuators for high density disk drives," M.S. thesis, Dep. Mech. Eng., Univ. California, Berkeley, May 1997.
- [9] S. Aggarwal, D. Horsley, R. Horowitz, and A. P. Pisano, "Microactuators for high density disk drives," in *Proc. Amer. Control Conf.*, Albuquerque, NM, June 1997, pp. 3979–3984.
- [10] G. Balas, J. Doyle, K. Glover, A. Packard, and R. Smith, *μ -Analysis and Synthesis Toolbox*, MUSYN and MathWorks, Inc., Natick, MA, 1995.
- [11] J.-Y. Yen, K. Hallamasek, and R. Horowitz, "Track-following controller design for a compound disk drive actuator," *ASME J. Dynam. Syst., Measur., Contr.*, vol. 112, pp. 391–402, Sept. 1990.

Toshiki Hirano received the B.S. degree in mechanical engineering and the M.S. degree in information engineering from the University of Tokyo, Tokyo, Japan, in 1988 and 1990, respectively.

In 1990, he joined the Tokyo Research Laboratory, IBM Japan, where he carried out a joint MEMS research program with the Institute of Industrial Science, University of Tokyo. In 1995, he joined the Almaden Research Center, IBM Corporation, San Jose, CA, where he is currently conducting research on the application of a microactuator to hard-disk drives.

Long-Sheng Fan (S'83–M'88) received the Ph.D. degree in electrical engineering and computer sciences from the University of California at Berkeley, in 1990.

In 1989, he joined the Almaden Research Center, IBM Corporation, San Jose, CA, as a Research Staff Member and has been conducting micromechanics research for information storage. He is currently a Project Leader in MEMS Technology, Interface Tribology, and Mechanics. He initiated the building of an Si CVD laboratory and set up a micromechanics characterization laboratory. He developed a multilayer, high-aspect-ratio micromechanical technology and a high-data-rate AFM cantilever/tip process for an exploratory 25 Gb/in² AFM recording. He is currently working on MEMS technology and devices for high-density information storage and on MEMS/HDD integration issues. His MEMS project team recently reported a record-breaking HDD servo bandwidth, using MEMS metal microactuators, making HDD track density possible well beyond 25 kTPI on the challenging 3.5-in platform.

Wen Y. Lee received the Ph.D. degree in physical chemistry from the University of Washington, Seattle, in 1975.

In 1975, he joined the Almaden Research Center, IBM Corporation, San Jose, CA. His main research interests are preparation, processing, and properties of various thin films, including thin films for optical and magnetic recording and high T_c superconducting thin films. He is currently conducting research in the area of advanced thin film materials for magnetic recording heads and disks, as well as high-aspect-ratio polymer etching for microactuator application.

John Hong received the B.S. degree from Montana State University, Bozeman, the M.S. degree from Syracuse University, Syracuse, NY, and the Ph.D. degree from North Carolina State University, Raleigh, all in electrical engineering.

In 1970, he joined IBM Corporation, where he is currently a Member of the Advanced Magnetic Recording Laboratory, Almaden Research Center, San Jose, CA. He has worked on circuit design, signal processing, and control system design for magnetic recording systems and local area networks. He is currently working on a dual-stage servo control system for very high track density disk drives and read/write signal processing for a high-data-rate magnetic recording channel.

Wayne Imano received the Ph.D. degree in physics from Purdue University, West Lafayette, IN.

In 1980, he joined the Almaden Research Center, IBM Corporation, San Jose, CA, to work in the areas of electrophotography, disk drive mechanics, and multilayer optical storage. His current research interests are the design and simulation of high-bandwidth actuators for disk drives.

Surya Pattanaik (M'94), photograph and biography not available at the time of publication.

Susanna Chan received the B.S. degree in biological sciences with a minor in chemistry from San Jose State University, San Jose, CA, in 1997.

In February 1997, she joined the Almaden Research Center, IBM Corporation, San Jose, CA, where she is working on MEMS microactuator process development, in which she primarily conducts research on high-aspect-ratio polymer etching, thick polymer spin coating, and photolithography.

Patrick Webb received the B.S. degree from the University of California at Berkeley, and the M.S. degree from Stanford University, Stanford, CA, both in materials science and engineering, in 1992 and 1995, respectively.

In 1991, he joined the Almaden Research Center, IBM Corporation, San Jose, CA, as a co-op student, eventually working in a variety of areas ranging from electroplating and photolithography to thin film ion beam deposition. During 1996–1997, he was a Volunteer with the U.S. Geological Survey at the Hawaiian Volcano Observatory on the island of Hawaii. In 1997, he joined the Microactuator Group at the Almaden Research Center to address process integration issues involved with the fabrication of a dual-stage microactuator. He is currently a Staff Engineer, responsible for thin-film ion beam deposition process development in the Storage Systems Division.

Roberto Horowitz (M'89), for a photograph and biography, see this issue, p. 155.

Sanjay Aggarwal, photograph and biography not available at the time of publication.



David A. Horsley received the B.S., M.S., and Ph.D. degrees in mechanical engineering from the University of California at Berkeley, in 1992, 1994, and 1998, respectively.

While at the University of California at Berkeley, he conducted research on micromechanical devices for data storage. He is currently with DiCon Fiberoptics, Berkeley, CA, where he is developing microfabrication techniques for optomechanical devices and designing passive optical components for fiberoptic communication systems.